CrossMark

RESEARCH ARTICLE

A hybrid finite-volume/finite-difference-based one-dimensional Boussinesq model for waves attenuated by vegetation

Soumendra Nath Kuiry[1] · Yan Ding[2]

Abstract A hybrid finite-volume/finite-difference scheme is proposed to solve the one-dimensional Boussinesq equations for wave attenuation by vegetation. The effect of vegetation is included as a source term in a form of drag force. The convective part of the equations is discretized by the finite-volume method, while the finite-difference method is used to discretize the remaining terms. The variable values for the local Riemann problem at each cell face are calculated by a fourth-order MUSCL reconstruction method. The source terms and the dispersion terms are discretized using the centered finite-difference schemes up to fourth-order accuracy. The unsteady terms are discretized by the second-order MUSCL-Hancock scheme. The discretized continuity equation is solved explicitly, while the discretized momentum equation is solved using the Thomas algorithm. The developed Boussinesq model is tested with analytical solutions and reported experimental data. To further validate the model, the computed results are compared with the experimental data observed in two vegetated wave flumes. It is demonstrated that the developed model is suitable for predicting wave propagation in vegetated water bodies.

✉ Yan Ding
ding@ncche.olemiss.edu

Soumendra Nath Kuiry
snkuiry@iitm.ac.in

[1] Environmental and Water Resources Engineering Division, IIT Madras, Chennai, TN 600 036, India

[2] National Center for Computational Hydroscience and Engineering, The University of Mississippi, University, MS 38677-1848, USA

List of symbols

A_v	Projected area of a vegetation stem normal to flow
b_v	Width of vegetation stem
C_D	Drag coefficient
F	Convective flux vector
F_v	Drag force per unit area
F	Flux vector at an interface
$\mathbf{F}_L$	Flux vector evaluated at the left-hand side of a cell interface
$\mathbf{F}_R$	Flux vector evaluated at the right-hand side of a cell interface
g	Gravitational acceleration
H	Water surface level from a datum
h, h_L, h_R	Flow depth, depths evaluated at the left- and right sides of a cell
h_{tol}	Water depth tolerance to define a dry cell
h_v	Length of vegetation stem
i	Cell index
$i \pm 1/2$	Cell interface indices
L, R	Left and right sides of a cell interface
S	Source term vector
S_0	Bed slope
S_f	Bed friction
$t, \Delta t$	Time and time step
t_v	Thickness of vegetation stem
U	Vector of conserved variables
u	Velocity
u_L, u_R	Velocities evaluated at the left- and right-hand sides of a cell interface
W	Thickness of sponge layer
ω	Angular velocity
x, y	Cartesian coordinate
Δx	Cell length

🦅 Springer

| z | Bed elevation from datum |
| η | Deviation of water surface from still water |

1 Introduction

Large amplitude waves induced by hurricanes and tsunamis in coastal water can inundate low-lying areas, causing casualties and damage to properties. The focus of recent trends for protecting coastal areas from such hazards is on non-intrusive measures, such as vegetation. Vegetation offers resistance to the incident waves, dissipates wave energy and surge, strengthens the soils through root systems and induces sediment deposition in the vegetated regions. Thus, vegetation plays an important role on attenuation of wave runup in a beach and its shoreline stability. Therefore, there is a need to improve knowledge on wave–vegetation interactions through experimentation and numerical analysis.

Different types of vegetation produce different amount of resistance to the shoreward propagating waves. A number of laboratory experiments and field measurements on different vegetation species have been carried out by many investigators over the time. The laboratory and field measurements have been used to understand the physical processes and to validate the mathematical models. Knutson et al. (1982) conducted a field study on wave damping in two *Spartina alterniflora* marshes located on the eastern shore of the Chesapeake Bay in Virginia, USA. Asano et al. (1988) and Kobayashi et al. (1993) conducted experiments on wave attenuation due to vegetation in a flume using flexible polypropylene strips as model vegetation. Schutten et al. (2004) measured the hydraulic forces on submerged aquatic vegetation by waves. Augustin et al. (2009) conducted laboratory experiments on wave attenuation using synthetic vegetation under a range of wave conditions and plant stem densities. Li and Yan (2007) conducted experiments on wave–current–vegetation interaction in a flume using semi-rigid rubber rods as model vegetation. Ozeren and Wren (2011) conducted a large number of experiments in a laboratory wave flume to examine and measure the resistance effect of artificial vegetation and live vegetation species collected from the Louisiana and Mississippi Gulf coasts. Their experimental conditions include various incident regular and random waves. These experiments have provided knowledge and understanding of the physical phenomena and the collected data have been widely used for validating mathematical models.

Considerable research efforts have been devoted over the years to the development of analytical and mathematical models to predict wave runup and its attenuation by vegetation. Many simulation models predict wave attenuation using time-averaged conservation equation of wave energy and account for vegetation effect as an energy dissipation term (Price et al. 1968). Knutson et al. (1982) concluded that wave attenuation is caused by energy loss through the work performed on the plants. Camfield (1983) considered vegetation as a high friction area and studied wind-wave growth over shallow flooded regions. Later on, the conservation of momentum approach was introduced to predict wave attenuation by vegetation (Kobayashi et al. 1993). In these studies, either analytical solutions of the governing equations obtained from the linear wave theory have been exploited, or simplified form of the momentum equation has been solved.

Wave attenuation due to vegetation can also be quantified by numerical modelling of free surface flows described by the fully three-dimensional (3D) Navier–Stokes equations considering resistance due to vegetation as a source term (e.g., Li and Yan 2007; Zhan et al. 2014). However, those numerical models based on the Navier–Stokes equations are very time-consuming and are not efficient for practical applications. The computationally more efficient long-wave models using the depth-averaged (or shallow water) equations are often preferred over the models based on the Navier–Stokes equations (Wu et al. 2013). Among them, the depth-averaged shallow water equations are valid only for non-dispersive long waves. For examples, Wu et al. (2001) and Thuy et al. (2010) developed or applied the two-dimensional (2D) shallow water models to study the impact of mangroves, coastal forests and instream vegetation on tsunami waves, tidal current and river flow, which are typical long waves. Due to the non-dispersive feature, the shallow water equations are also not suitable for modelling wave deformation and transformation from relatively deep water to shallow water and when the propagating waves are short in nature. This situation is common, especially in the case of experiments conducted in laboratory flumes. In these circumstances, another class of numerical models based on the solution of the extended Boussinesq equations is a suitable choice.

The pioneering work of Peregrine (1967) established the foundation of many Boussinesq-type models used today. However, the equations were restricted to relatively shallow-water depths, i.e., the water depth had to be less than one-fifth of the wave-length to keep errors in the phase velocity to less than 5 %. Madsen et al. (1991) enhanced the classical Boussinesq equations by introducing third-order terms with a free parameter into the momentum equation. Nwogu (1993) was the pioneer who derived a new set of governing equations from the three-dimensional Euler equations with the horizontal velocity evaluated at a reference depth. These equations have errors of less than 2 % in the phase velocity from the shallow-water depths up to the deep water limit. However, Nwogu (1993) optimized form of the equations which limit the ability of the equations to describe highly nonlinear waves in shallow water and this led Wei and Kirby (1995) to derive a fully nonlinear form of the equations. The fully nonlinear

equations are particularly useful for simulating highly asymmetric waves in shallow water, wave-induced currents, wave setup close to the shoreline and wave–current interaction. Later, Nwogu (1993) extended the fully nonlinear Boussinesq equations to the surf zone, by coupling the mass and momentum equations with a one-equation turbulence model for simulating the temporal and spatial evolution of the turbulent kinetic energy produced by wave breaking. The resulting numerical model and its unique capabilities were demonstrated in numerous prototype applications by Nwogu and Demirbilek (2001). The above two approaches have identical dispersion characteristics that show good agreement with linear wave theory. Tonelli and Petti (2009) and Tonelli and Petti (2010) proposed a hybrid scheme for the extended Boussinesq equations of Madsen and Sørensen (1992) for slowly varying bathymetry. Their numerical code combines the finite-volume technique applied to solve the advective part of the equations and the finite-difference method to discretize the dispersive and the source terms.

Shiach and Mingham (2009) explored the accuracy of a second-order discretization of the unsteady term in the extended Boussinesq equations unlike the fourth-order discretization of the unsteady term (Tonelli and Petti 2009). They concluded that second-order accurate discretization for time and up to fourth-order accurate discretization in space provide sufficient accuracy for the Boussinesq equations proposed in Madsen and Sørensen (1992). Meanwhile, Shi et al. (2012) presented a high-order TVD solver using the HLL scheme (Harten 1983) for the Boussinesq equations. The study shows that the Riemann solver-based approach can successfully simulate breaking and non-breaking wave propagation. However, these Boussinesq equations-based models did not consider the effects of vegetation. In recent years, the Boussinesq-type models have been used to simulate decay in wave height due to vegetation. The Riemann solver-based solution approaches for the Boussinesq equations with vegetation effect are highly limited. The main advantage of the Riemann-solver-based approaches is that the breaking-wave propagation can be computed without considering extra efforts for wave breaking phenomenon (Tonelli and Petti 2009, 2010). Therefore, the underlying motivation of this research is to develop a Riemann solver-based computationally stable and robust hybrid solution scheme for applications of the Boussinesq models to wave dissipation in heavily vegetated coastal areas. To achieve this goal, the Boussinesq equations presented in Shiach and Mingham (2009) were modified to include a drag force term that represents the resistance of vegetation as a source term in the momentum equation. A hybrid finite-volume/finite-difference method was used to solve the resulting governing equations for breaking and non-breaking waves. The model has been verified and validated with analytical solutions and experimental data. The governing equations, numerical schemes, verification
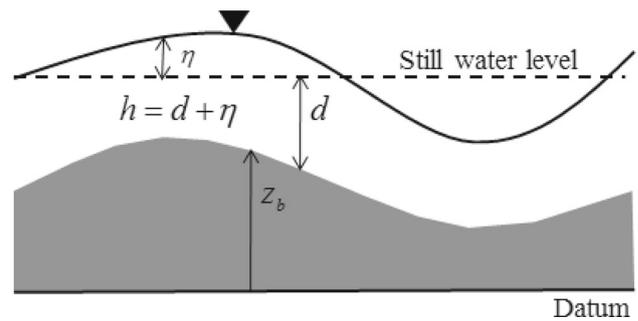
Fig. 1 Definition sketch of free surface flow problem

and validation of the model are described in the following sections.

2 Governing equations

In this section, the Boussinesq equations (Shiach and Mingham 2009) are extended to take into account the effect of vegetation and rewritten in the conservative form so that a hybrid finite-volume/finite-difference scheme can be used. Figure 1 provides the definition sketch of the free surface flow problem, in which d denotes the still water depth, η the free surface elevation above the still water level, h the water depth $(d + \eta)$, and z_b the bed elevation from a datum. Including the vegetation drag force term, the resulting one-dimensional (1D) Boussinesq equations are given by

$$\frac{\partial \eta}{\partial t} + \frac{\partial (hu)}{\partial x} = 0 \tag{1}$$

$$\frac{\partial (hu)}{\partial t} + \frac{\partial (hu^2)}{\partial x} + gh\frac{\partial \eta}{\partial x} + \frac{\partial \psi}{\partial x} + ghS_f + F_D + F_{sp} = 0 \tag{2}$$

where u is the depth-averaged horizontal velocity, S_f is the friction slope $S_f = n^2 u\,|u|/h^{4/3}$ with n being the Manning's roughness coefficient, F_D denotes the drag force per unit area induced by vegetation, F_{sp} is the energy dissipation in the sponge layer that is described later, and the term ψ accounts for wave dispersion:

$$\frac{\partial \psi}{\partial x} = -\left(B + \frac{1}{3}\right)d^2\frac{\partial^3(hu)}{\partial x^2 \partial t} - Bgd^3\frac{\partial^3 \eta}{\partial x^3}$$
$$-d\frac{\partial d}{\partial x}\left(\frac{1}{3}\frac{\partial^2(hu)}{\partial x \partial t} + 2Bgd\frac{\partial^2 \eta}{\partial x^2}\right) \tag{3}$$

where B is a free parameter that determines the dispersion properties of the system. Madsen and Sørensen (1992) has suggested a value of $B = 1/15$.

By assuming that the bathymetry remains constant over time or changes much slower than the water surface, the continuity and momentum equations, Eqs. (1) and (2), can be rewritten in the conservative form as:

$$\frac{\partial \mathbf{U}}{\partial t} + \frac{\partial \mathbf{F}(\mathbf{U})}{\partial x} = \mathbf{S} \qquad (4)$$

where $\mathbf{U}$ and $\mathbf{F}(\mathbf{U})$ are vectors containing the conserved variables and fluxes, respectively, and $\mathbf{S}$ is the vector of source terms:

$$\mathbf{U} = \begin{bmatrix} h \\ \Phi(hu) \end{bmatrix}; \quad \mathbf{F} = \begin{bmatrix} hu \\ hu^2 + \frac{1}{2}gh^2 \end{bmatrix};$$

$$\mathbf{S} = \begin{bmatrix} 0 \\ gh(S_o - S_f) - F_D - F_{sp} + S_d \end{bmatrix} \qquad (5)$$

where S_0 is the bed slope. The provisional variable $\Phi(hu)$ and the source term S_d are expressed as:

$$\Phi(hu) = hu - \left(B + \frac{1}{3}\right) d^2 \frac{\partial^2(hu)}{\partial x^2} - \frac{1}{3}d\frac{\partial d}{\partial x}\frac{\partial(hu)}{\partial x}$$

$$S_d = Bgd^3 \frac{\partial^3 \eta}{\partial x^3} + 2Bgd^2 \frac{\partial d}{\partial x}\frac{\partial^2 \eta}{\partial x^2}$$

The quadratic vegetation drag force is determined by

$$F_D = \frac{1}{2}C_D N_v A_v u_v |u_v| \qquad (6)$$

where u_v is the velocity acting on the vegetation elements which is same as the depth-averaged velocity of the flow, C_D is the drag coefficient, N_v is the number of stems per unit area, and A_v is the projected area of a stem normal to the flow direction. Because vegetation may be emergent or submerged, the projected area and volume of the wetted portion should be used in calculating the drag force. If the vegetation element is approximated as a cylindrical stem, the wetted projected area and volume are expressed as:

$$A_v = D_v \min(h_v, h), \quad V_v = \frac{\pi D_v^2}{4}\min(h_v, h) \qquad (7)$$

where D_v is the representative diameter of the vegetation element, and h_v is the vegetation height, and h is depth of flow. Equation (7) makes sure that the projected area and volume for calculating drag force (Eq. 6) are calculated only for the height of vegetation that is under water. For partially submerged vegetation, D_v represents the diameter of the wetted portion. In general, D_v can be interpreted as the nominal diameter of the stem that is related to the stem volume V_v by $D_v = \sqrt{4V_v/\pi \min(h_v, h)}$. More details on how to approximate vegetation elements can be found in Wu (2007). For emergent vegetation, the acting flow velocity u_v is the depth-averaged flow velocity u. For submerged vegetation, u_v is the average velocity in the vegetation layer and can be determined using Stone and Shen's method (Stone and Shen 2002),

$$u_v = \eta_v u \left(\frac{h_v}{h}\right)^{1/2} \qquad (8)$$

where η_v is a coefficient of about 1.0. The use of Eq. (8) is explained in detail in Wu (2007).

3 Numerical methods

The Boussinesq equations given in Eqs. (1) and (2) are solved using a hybrid method in which a finite-volume scheme is applied to the conservative part and a finite-difference scheme is applied to the remaining terms. The hybrid method has fourth-order accuracy in space and second-order accuracy in time (Shiach and Mingham 2009). The spatial integration of Eq. (4) over a cell with a length of Δx and applying the divergence theorem to the second term yields

$$\int_{\Delta x} \frac{\partial \mathbf{U}}{\partial t}dx + \oint_{\Gamma} \mathbf{F} \cdot \mathbf{n}_m d\Gamma = \int_{\Delta x} \mathbf{S}dx \qquad (9)$$

where $\mathbf{n}_m$ is the outward pointing normal vector of side m, Γ is the boundary of the cell. Equation (9) can be further approximated as:

$$\frac{\partial \mathbf{U}}{\partial t}\Delta x + \sum_{m=1}^{M}(\mathbf{F} \cdot \mathbf{n}_m) = \mathbf{S}\Delta x \qquad (10)$$

where M is the number of faces at each cell and is equal to 2 for the present 1D model. The time integration, discretization of the intercell fluxes and the source terms in Eq. (10) are described in the following subsections.

3.1 Riemann fluxes and fourth-order MUSCL reconstruction

To handle wave breaking, the finite-volume scheme requires the solution of a local Riemann problem at each cell interface and, therefore, the HLL approximate Riemann solver (Harten 1983) is used to compute the convective fluxes. The HLL Riemann solver is preferred because it can represent the flux for dry bed situation and does not require any entropy fix. Wei and Kirby (1995) pointed out that a fourth-order accurate treatment of the first-order spatial derivatives is required so that the truncation error in the numerical scheme is smaller than the dispersion terms present in the model. To calculate the conserved variables at each cell interface for the Riemann flux computation, the fourth-order MUSCL reconstruction proposed by Yamamoto et al. (1998) is implemented in this study. For smooth reconstruction of water surface at a cell interface, the surface gradient method suggested by

Zhou et al. (2001) is used, in which the water surface elevation rather than water depth is used as the state variable.

3.2 Source terms

A cell-centered discretization is used for the bed slope, bed friction and vegetation drag force terms. The bed elevation at the cell interface is obtained simply by linear interpolation of the elevations at the two neighbouring cell centres. A fourth-order central difference approximation is used for the first derivative and second- and third-order central differences for the second and third spatial derivatives in the dispersion terms. The discretized source term of the momentum equation for cell i takes the following form:

$$S_i = -gh_i \left(\frac{z_{b,i+1/2} - z_{b,i-1/2}}{\Delta x} \right) - gh_i S_{fi} - F_{Di}$$
$$+ \frac{Bgd_i^3}{2\Delta x^3}(-\eta_{i-2} + 2\eta_{i-1} - 2\eta_{i+1} + \eta_{i+2})$$
$$+ \frac{Bgd_i^3}{6\Delta x^3}(d_{i-2} - 8d_{i-1} + 8d_{i+1} - d_{i+2})$$
$$\times (\eta_{i-1} - 2\eta_i + \eta_{i+1}) + \omega D_s(hu)_i \qquad (11)$$

3.3 Time integration

The time discretization is generally based on a high-order predictor–corrector approach. According to Shiach and Mingham (2009), the second-order accurate MUSCL-Hancock scheme provides sufficient accuracy with less computational cost and is thus adopted in this study. It uses two-stage predictor and corrector method. The predictor step determines the intermediate values over a half time step as:

$$\mathbf{U}^{t+1/2} = \mathbf{U}^t - \frac{\Delta t}{2\Delta x}\left[\sum_{m=1}^{M} \mathbf{F}(\mathbf{U}_m)^t \cdot \mathbf{n}_m \right] \qquad (12)$$

where t and $t+1/2$ denote the current and intermediate values and Δt is the time step. The corrector steps provide the full conservative solution over a time step, as given by

$$\mathbf{U}^{t+1} = \mathbf{U}^t - \frac{\Delta t}{\Delta x}\left[\sum_{m=1}^{M} \mathbf{F}(\mathbf{U}_m^L, \mathbf{U}_m^R)^{t+1/2} \cdot \mathbf{n}_m \right] + \Delta t\mathbf{S} \quad (13)$$

where $\mathbf{F}(\mathbf{U}_m^L, \mathbf{U}_m^R)$ is the flux at the cell interface m, the values of which are obtained by the HLL Riemann solver and $\mathbf{U}_m^L$ and $\mathbf{U}_m^R$ are the values of the conserved variables at the cell interface obtained using the fourth-order MUSCL reconstruction method proposed in Yamamoto et al. (1998).

The value of the time step size, Δt, is restricted using the CFL condition as suggested in Shiach and Mingham (2009).

3.4 Evaluation of velocity

The velocity function $\Phi(hu)$ in Eq. (5) is discretized using the second-order accurate central differences for the first- and second-order derivatives, resulting in

$$\Phi(hu)_i = (hu)_i - \left(B + \frac{1}{3} \right) d_i^2$$
$$\times \left[\frac{(hu)_{i-1} - 2(hu)_i + (hu)_{i+1}}{\Delta x^2} \right]$$
$$- \frac{1}{3}d_i \left(\frac{-d_{i-1} + d_{i+1}}{2\Delta x} \right)\left[\frac{-(hu)_{i-1} + (hu)_{i+1}}{2\Delta x} \right]$$
$$(14)$$

which can be factorized to give

$$\Phi(hu)_i = a_i(hu)_{i-1} + b_i(hu)_i + c_i(hu)_{i+1} \qquad (15)$$

where

$$a_i = -\frac{(B + 1/3)d_i^2}{\Delta x^2} + \frac{d_i}{12\Delta x^2}(-d_{i-1} + d_{i+1})$$
$$b_i = 1 + \frac{2(B + 1/3)d_i^2}{\Delta x^2}$$
$$c_i = -\frac{(B + 1/3)d_i^2}{\Delta x^2} - \frac{d_i}{12\Delta x^2}(-d_{i-1} + d_{i+1})$$

The coefficients a_i, b_i and c_i in Eq. (14) are time independent and hence they are evaluated once and used throughout the simulation. Equation (15) forms a linear system of equation with a tri-diagonal matrix, which can be efficiently solved using the Thomas algorithm (Thomas 1979).

4 Boundary conditions

Various boundary conditions have been implemented in the developed Boussinesq wave model, including a non-reflecting wave boundary, a moving boundary due to wave runup and rundown over a sloping beach, and a sponge layer boundary to absorb wave energy at the end of the flume. Characteristic boundary conditions have been used at subcritical inlet or outlet where either water depth or velocity is known and the unknown variable is calculated from the characteristic equation (Kuiry et al. 2012). The non-reflecting wave boundary, moving boundary and sponge layer boundary conditions used in the present model are discussed briefly in the following subsections.

4.1 Non-reflecting boundary condition at wave entrance

When incident waves are imposed as a time series of water level, reflection may take place after they hit a land bound-

ary at the other end of the domain. The reflected waves may interfere with the incident waves. This is why a non-reflecting wave inlet boundary condition as suggested in Hu et al. (2000) is implemented to pass the reflected waves freely through the inlet. In the characteristic equation while imposing incident wave height, the reflected wave height is also added in the expression for celerity. The reflected wave height is calculated assuming long waves in shallow water. This type of boundary allows reflected waves to pass freely through the inlet while imposing incident waves and this approach generally works well. Its accuracy and efficiency are demonstrated in Hu et al. (2000).

4.2 Moving boundary on the shoreline

Wave runup and rundown on a sloping beach is a moving boundary problem that can be viewed as wetting and drying of boundary cells. A threshold water depth, h_{tol} (generally, 10^{-3} m or less), is used to determine wetting or drying. At each time step, the cells are checked for dry and wet definition. The cells having water depths less than h_{tol} are defined as dry; otherwise, the cells are wet. The moving boundary is defined as the line of separation between wet and dry cells. If a cell that has at least one neighbouring wet cell is included in the flux computation. However, the dry cells that do not have any wet neighbouring cell are not considered in the computation at a time step (Kuiry et al. 2012; Que and Xu 2005).

4.3 Sponge layer boundary

For many laboratory experiments, wave absorber is usually installed in the downwave end of the flume to reduce the wave reflection. In a numerical model, an equivalent concept is to implement a sponge layer in the downwave end of the computational domain. The energy dissipation in the sponge layer is calculated as:

$$F_{sp} = \omega D_s(hu) \tag{16}$$

where ω is the angular frequency which can be calculated from the given wave period, and D_s is a coefficient defined by

$$D_s = \begin{cases} \frac{\exp(w_s/W)-1}{\exp(1)-1}, & \text{inside the sponge layer} \\ 0, & \text{outside the sponge layer} \end{cases}$$

where w_s is the distance from the starting point of the sponge layer, and W is the length of the sponge layer. In the test examples presented herein, the W is set at 2.5 time the wave length which reduces wave reflection significantly.

5 Tests and results

The present numerical Boussinesq model has been validated in a two-step test approach: first, the proposed model is first tested for regular wave propagation without considering vegetation in the flow domain. Then, the model is applied to reproduce laboratory experiments on wave attenuation by vegetation. In the following section, we present three validation results without vegetation by simulating solitary wave propagation in a straight and flat wave flume, wave runup in a sloping beach, and wave deformation over a submerged bar. After the numerical model has been confirmed that it is accurate enough to compute wave deformation and transformation without vegetation, two model test cases with vegetation have been conducted: one case is based on the experimental results done by Asano et al. (1988); another is the recent laboratory study by Ozeren and Wren (2011). All the computational results of the proposed model presented here are the convergent or best numerical results, for which we have tested the effects of different time steps (Δt) and grid sizes (Δx).

5.1 Solitary wave propagation in a horizontal channel

A solitary wave retains its amplitude, shape and speed as it travels down a flat-bed channel due to balance between the nonlinear terms that steepen the wave and the dispersion terms that flatten the wave. This classical example is used herein to test capability of the model to simulate such a phenomenon. The initial values of η and u are defined as (Wei and Kirby 1995):

$$\eta = A_1 \sec h^2 [B(x - Ct)] + A_2 \sec h^4 [B(x - Ct)] \tag{17}$$
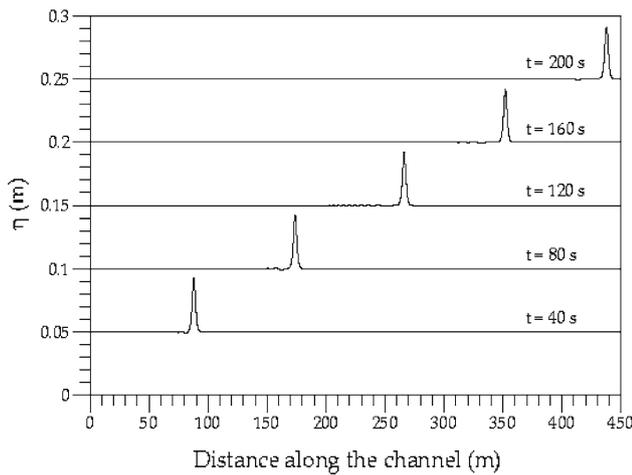
$$u = A \sec h^2 [B(x - Ct)] \tag{18}$$

where

$$A = \frac{C^2 - gd}{C}$$

$$B = \left(\frac{C^2 - gd}{4d^2 \left[(\alpha + 1/3)gd - \alpha C^2 \right]} \right)^{\frac{1}{2}}$$

$$A_1 = \frac{C^2 - gd}{3[(\alpha + 1/3)gd - \alpha C^2]} d$$

$$A_2 = -\frac{(C^2 - gd)^2}{2gdC^2} \frac{[(\alpha + 1/3)gd + 2\alpha C^2]}{[(\alpha + 1/3)gd - \alpha C^2]} d$$

The channel is 450 m long, with a constant water depth $d = 0.45$ m. The channel is discretized using $\Delta x = 0.01$ m and a stable time step of $\Delta t = 0.001$ s is used for the simulation. The solitary wave with an amplitude of 0.045 m is generated
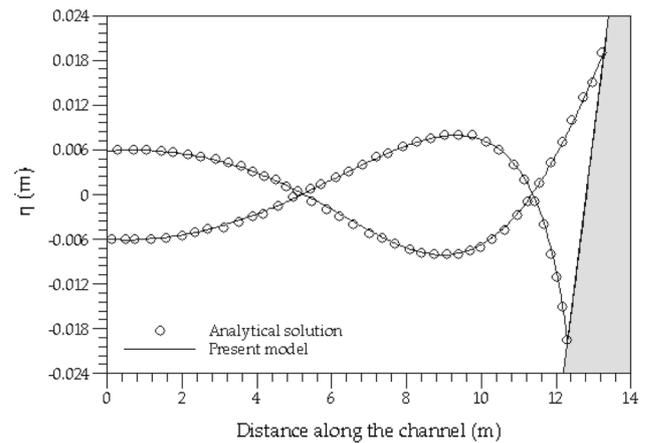
Fig. 2 Solitary wave propagation in a channel

Fig. 3 Maximum and minimum sine wave runup on a sloping beach. *Grey area* represents the beach in distorted scale

at the inlet with a phase speed of $C = 2.203$ m/s. The solutions obtained using the present Boussinesq model at times $t = 40, 80, 120, 160$ and 200 s are shown in Fig. 2. The shape and amplitude of the computed solitary wave remain almost constant. The error in peak at $t = 200$ s, after the solitary wave has travelled a distance of 437 m, is 7 %, indicating that the numerical scheme successfully retains the dispersion present in the governing equations. However, the results show that a train of small waves is generated behind the solitary wave. This is the consequence of specifying the low-order approximation of the velocity obtained from the analytical solution to the model as initial condition and can be avoided if high-order approximation of velocity from the numerical model is used as initial condition (Tonelli and Petti 2009). Tonelli and Petti (2010), in their successive study, placed a rightward moving solitary wave and used the numerical solution as the initial condition when the wave crest was at the distance of 100 m from the inlet. With this initial condition, the wave starts propagating along the numerical channel and they were able to eliminate oscillations to a great extent.

5.2 Sine wave runup on a sloping beach

A benchmark test for the validation of moving boundary condition is considered here. This case also helps to examine the accuracy of the non-reflective inlet boundary condition. The numerical model is applied to simulate runup/rundown motion of a monochromatic wave train on a sloping beach. The model parameters are identical to those used in Lynett et al. (2002). This configuration has analytical solution, which was derived in Carrier and Greenspan (1958) using the hodograph transformation to solve the shallow water equations. A sine wave train with amplitude of 0.003 m and a period of 10 s propagates in a channel with initial water depth of 0.5 m and climbs up a 1:25 sloping beach. The

domain is discretized using a grid size of $\Delta x = 0.045$ m. A constant stable time step size of $\Delta t = 0.005$ s is used for the entire simulation. At the inlet, non-reflecting boundary condition is imposed to reduce the wave reflectivity and at the downstream moving boundary condition is used. Figure 3 compares the computed free surface against the analytical solution presented in Carrier and Greenspan (1958) for the maximum and minimum runup. The agreement between computed and analytical solutions is good.

5.3 Regular wave propagation over a submerged bar

A laboratory test case introduced by Dingemans (1987) is selected herein to examine the accuracy of the present model. The experiments were conducted in a 23 m long straight flume with a submerged bar and initial still water depth $d = 0.4$ m. The bar consisted of a 1:20 front slope and a 1:10 back slope separated by a level plane of 2 m in length, as shown in Fig. 4. The waves were generated with three different wave configurations (Table 1). Configurations A and C generated non-breaking waves, whereas Configuration B generated spilling breakers over the plane surface of the bar. Waves steepened along the front slope due to the nonlinear effects, whilst the back slope caused waves to break up into individual waves travelling at their own speeds. Water surface elevations over time were recorded at gages placed at $x = 2.0$ m (G1), $x = 5.7$ m (G2), $x = 10.5$ m (G3), $x = 13.5$ m (G4), $x = 15.7$ m (G5) and $x = 19.0$ m (G6).

The computational flume is discretized using a spatial step of $\Delta x = 0.01$ m and a time step of $\Delta t = 0.001$ s for all the cases. Manning's roughness coefficient is 0.001 m$^{-1/3}$s considering the smooth bottom surface. The regular waves are generated at the inlet boundary and a sponge layer is employed at the downstream end. Figures 5, 6 and 7 compare the water surface elevations at different gages obtained from
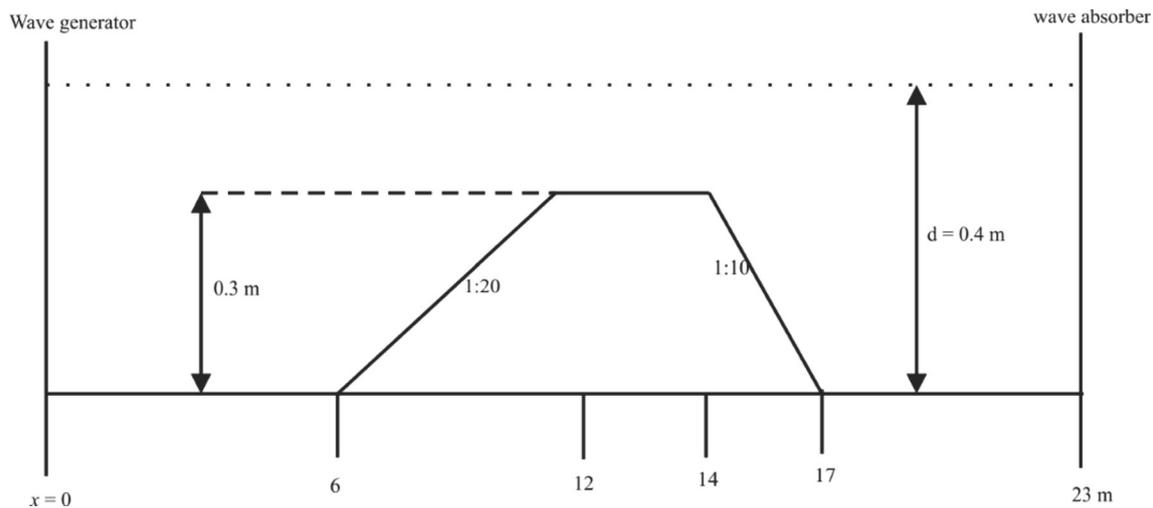
Fig. 4 Bed topography definition for regular wave propagation over a submerged bar

Table 1 Laboratory wave configurations used by Dingemans (1987)

Configuration	Wave height (m)	Period (s)	d/L
A	0.020	2.020	0.11
B	0.029	2.525	0.08
C	0.041	1.010	0.27

the experiments, the present model and Shiach and Mingham (2009) for the wave configurations A–C. It appears that there is phase error at gauge G2 but similar results have been reported in literature (on pages 41–42, Shiach and Mingham 2009), and they suggest that the error is associated with the recording of the experiments at this gauge.

The computed time series of water surface elevation at different gauges have been analyzed by calculating the mean absolute percentage error (MAPE) and mean absolute error (MAE), except G2,

$$\text{MAPE} = \frac{1}{N} \sum_{i=1}^{N} \left| \frac{\eta_{\text{obs}} - \eta_{\text{cal}}}{\eta_{\text{obs}}} \right|, \quad (19)$$

$$\text{MAE} = \frac{1}{N} \sum_{i=1}^{N} |\eta_{\text{obs}} - \eta_{\text{cal}}|, \quad (20)$$

where N is the total number of data, η_{obs} the observed water level, and η_{cal} the computed water level. The data at 0.1 s interval are compared for the experimental, Shiach and Mingham (2009) and the present model. The analysis indicates how closely the numerical model predicts the experimental water surface elevations (Tables 2, 3, 4). The gauges G4 and G6 show maximum MAPE errors for all the three configurations. This is due to the fact that there are considerable differences between the observed and simulated data for some time intervals though these differences are in mm

scale and the water surface elevations are very small. Again, there are differences between Shiach and Mingham (2009) and the simulated results but the differences are in mm scale. Therefore, though the MAPE and MAE differences are large, the differences in magnitudes are very small. However, the modelling of wave configuration (b) shows the worst agreement. This might be due to breaking of very small amplitude waves and we may need a vertical 2D or 3D model.

5.4 Wave attenuation due to vegetation in a laboratory flume (Asano et al. 1988)

The experiments conducted by Asano et al. (1988) are used here to test the accuracy of the Boussinesq wave model for wave attenuation caused by vegetation. The experiments were conducted in a wave tank of 27 m long, 0.5 m wide and 0.7 m high. The artificial vegetation was made of 0.25 m long, 0.052 m wide and 0.3 mm thick polypropylene strips, with a specific gravity of 0.9. The strips were bound to a wire net at the bottom of the wave flume. The length of vegetation field was 8 m. The capacitance wave gages were used to measure the free surface oscillations at four locations. A series of 60 test runs were conducted, out of which two are chosen for testing the present model. The following experimental conditions are selected: (a) wave height (H_{w}) = 0.113 m, period (T) = 1.25 s, d = 0.52 m and N_{V} = 1490 m^{-2}; and (b) H_{w} = 0.086 m, T = 2 s, d = 0.45 m and N_{V} = 1110 m^{-2}. These conditions were also considered by Li and Yan (2007) and their results are also presented for comparison.

The numerical model is set up to replicate the experimental conditions using a shorter length channel to reduce computation time by specifying the observed data as inlet and outlet boundary conditions. The computational domain is 12 m long and 1 m wide, Δx = 0.01 m, Δt = 0.001 s
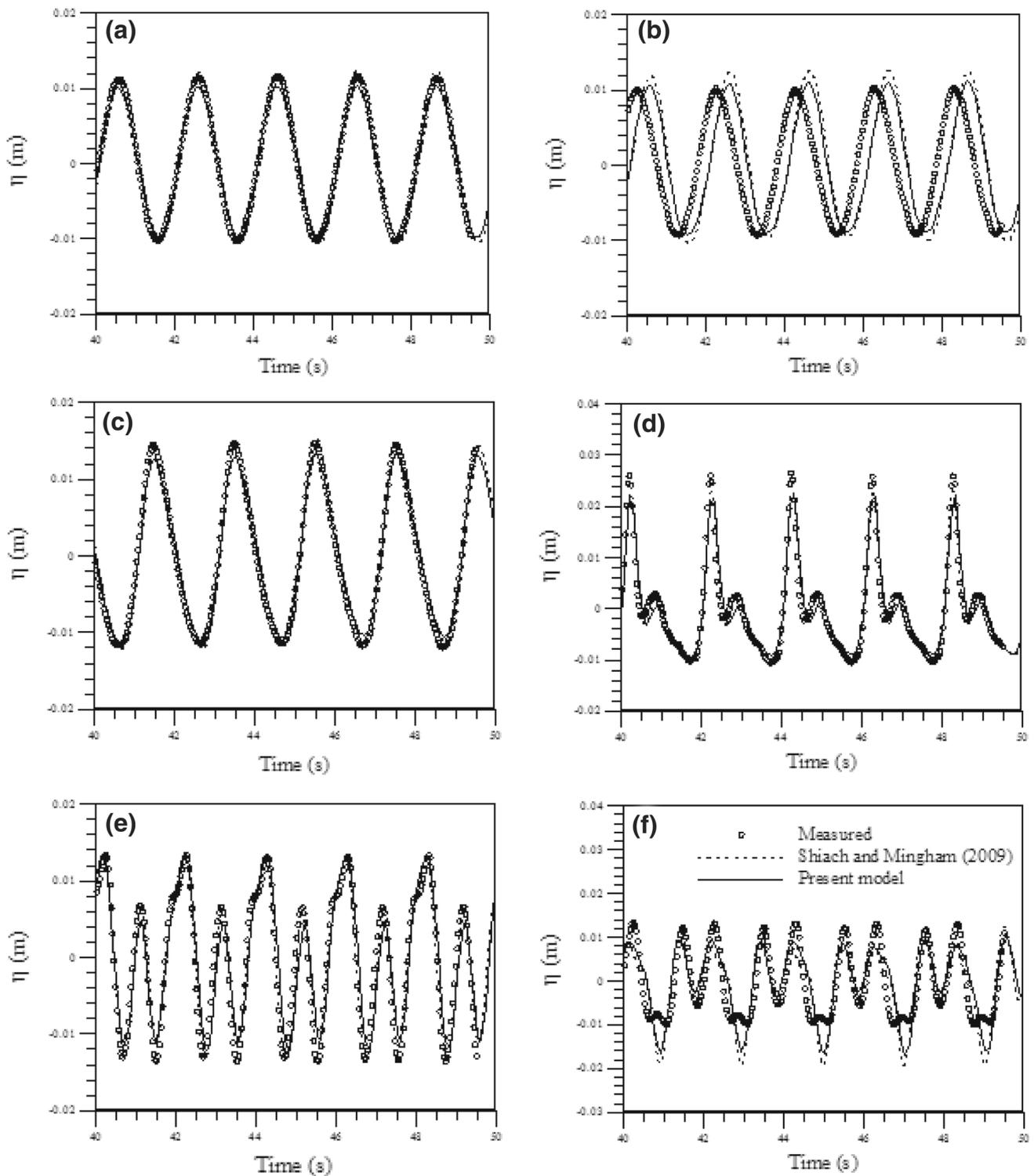
Fig. 5 Comparison of water surface elevations at different gages for Case 1: **a** G1, **b** G2, **c** G3, **d** G4, **e** G5 and **f** G6

and value of Manning's $n = 0.01$ are used. A non-reflecting boundary condition is specified at the inlet and a sponge layer is defined at the outlet. A sine wave train is introduced at the inlet and the simulation is carried out for sufficiently

long time so that a well-developed flow situation is obtained in the flow domain. The wave height at a point is obtained by subtracting the minimum water level from the maximum water level when dynamic steady state is reached at that
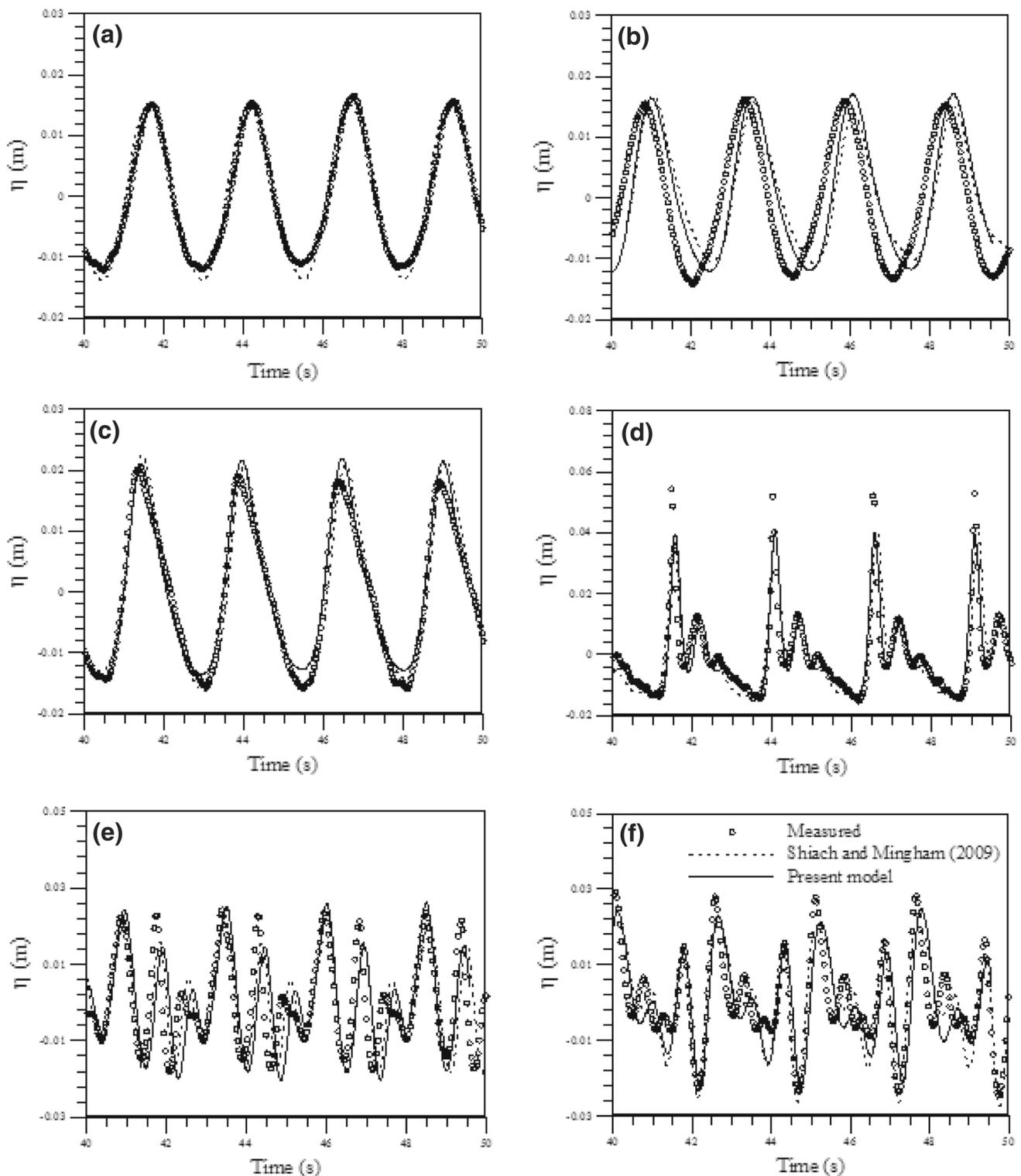
Fig. 6 Comparison of water surface elevations at different gages for Case 2: **a** G1, **b** G2, **c** G3, **d** G4, **e** G5 and **f** G6

point. The longitudinal wave height profiles obtained from the present model are compared with the numerical results of Li and Yan (2007) and experimental data (Asano et al. 1988) as shown in Fig. 8. While plotting, the origin is con-

sidered to be at the seaward side of the vegetation field. The C_d values for the plotted results are 0.18 and 0.15 for the cases (a) and (b), respectively. It should be noted that the C_d values are slightly larger than those in Li and Yan (2007)
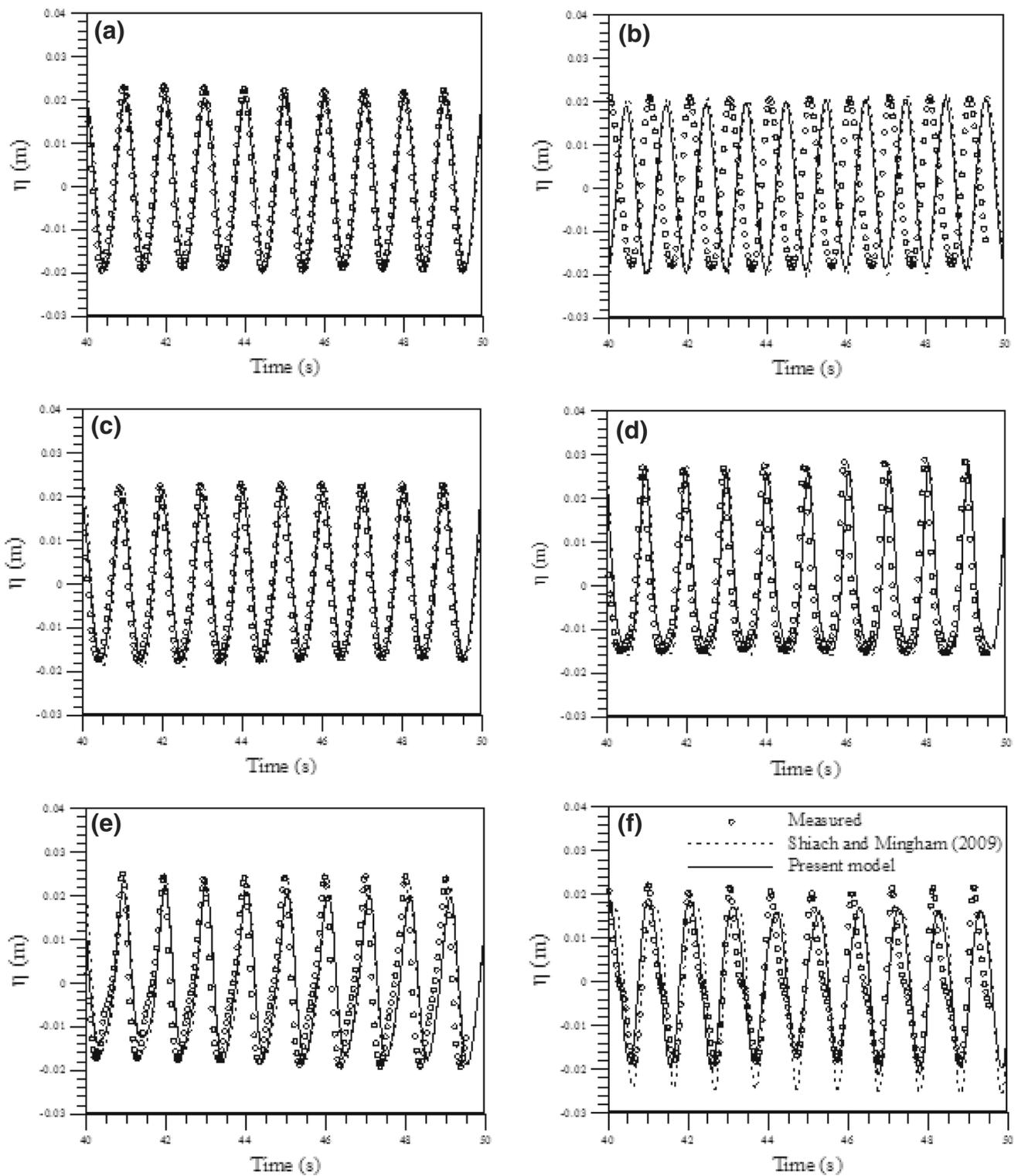
Fig. 7 Comparison of water surface elevations at different gages for Case 3: **a** G1, **b** G2, **c** G3, **d** G4, **e** G5 and **f** G6

and the probable reason is explained in the next test case. Figure 8 shows that the wave attenuation predicted by the present model closely follows the experimental observation with insignificant error (Table 5). The present model results exhibit slight wave reflection in the second case, which was also reported by Li and Yan (2007).

Table 2 Comparison of errors in predicting water surface elevations at different gages for wave configuration (A)

Gage	Shiach and Mingham (2009)		Present model	
	MAPE	MAE	MAPE	MAE
G1	3.76	0.0004	7.71	0.0008
G3	3.52	0.0004	9.32	0.0012
G4	49.72	0.0039	48.64	0.0044
G5	6.70	0.0008	17.16	0.0017
G6	53.37	0.0048	54.84	0.0048

Table 3 Comparison of errors in predicting water surface elevations at different gages for wave configuration (B)

Gage	Shiach and Mingham (2009)		Present model	
	MAPE	MAE	MAPE	MAE
G1	12.91	0.0016	13.55	0.0017
G3	6.44	0.0011	13.28	0.0022
G4	87.98	0.0049	83.30	0.0040
G5	43.27	0.0031	47.51	0.0035
G6	106.17	0.0011	90.31	0.0009

Table 4 Comparison of errors in predicting water surface elevations at different gages for wave configuration (C)

Gage	Shiach and Mingham (2009)		Present model	
	MAPE	MAE	MAPE	MAE
G1	8.99	0.0018	7.04	0.0014
G3	11.70	0.0020	6.62	0.0011
G4	15.54	0.0027	12.77	0.0023
G5	10.47	0.0021	15.62	0.0031
G6	38.13	0.0071	19.19	0.0037

5.5 Wave attenuation due to vegetation in a laboratory flume (Ozeren et al. 2011)

The 1-D Boussinesq wave model is also tested with data from the experiments conducted in a 20.6 m long, 0.5 m wide, and 1.22 m high wave flume at the USDA-ARS, National Sedimentation Laboratory, Oxford, Mississippi, USA (Ozeren and Wren 2011). A flap-type wave maker was used to generate waves of different amplitudes and periods (Table 6). At the downstream of the experimental setup, wave reflection was significantly reduced using a porous plastic cover and cottons below it. Such arrangements in the setup act as wave absorber. The model vegetation was constructed using 0.63 m long and 9.5 mm diameter wooden dowels. The dowels were fixed to the bottom of the flume by sliding them through the holes of perforated PVC sheets in a staggered pattern. The length of the vegetation field was $L_V = 3.66$ m, the stem den-
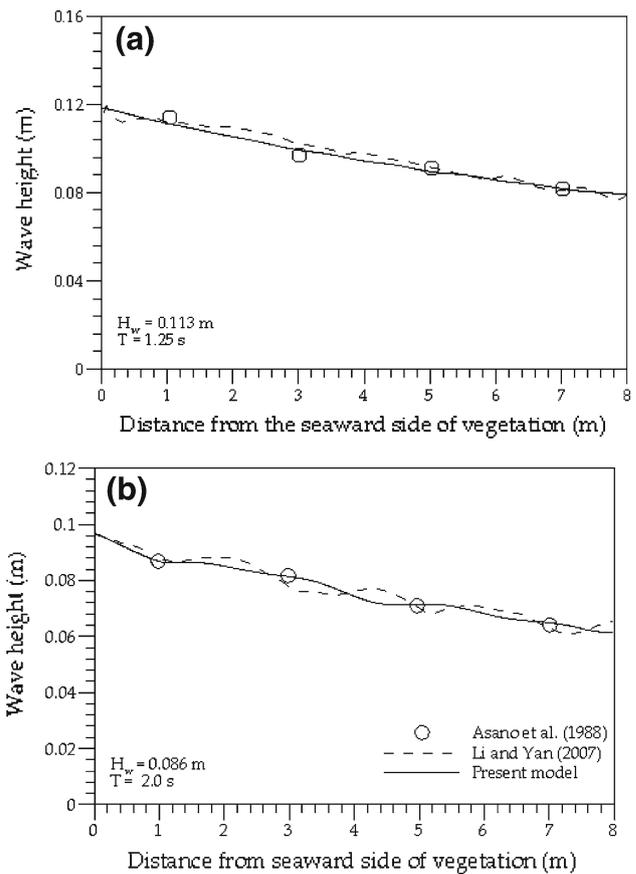
Fig. 8 Wave attenuation by vegetation (**a**) compared with Asano et al. (1988)

Table 5 Error values in predicting wave height

Test case	Experimental values			
	G1	G2	G3	G4
Case (a)	0.114	0.097	0.091	0.081
Case (b)	0.087	0.082	0.071	0.064
	% Error in wave height			
Case (a)	2.24	2.03	1.71	0.26
Case (b)	0.15	0.52	1.00	1.08

sity was 350 m^{-2} and the still water depth in the wave flume was, $d = 0.7$ m. All the test cases were well within the limit of the Boussinesq approximation, i.e., the depth to wave length (d/L) ratio was less than 0.5. Five gages were placed at different locations at $x = 3$ m (G1), $x = 11$ m (G2), $x = 12.5$ m (G3), $x = 14$ m (G4) and $x = 15.5$ m (G5) to record the water surface elevations over time, as shown in Fig. 9.

The first gage shows some discrepancy with the prescribed wave parameters to the wave maker and hence the computational domain is set to 15.5 m long and 1 m wide. The inlet is at the location of the second gage and a sponge layer is provided after the fifth gage, thus the computational domain is 7.2 m

long including the sponge layer. Since the wave flume bed was made of glass, the value of Manning's roughness coefficient at the bottom is set to $0.012\,\mathrm{m}^{-1/3}\mathrm{s}$. The spatial domain is represented by a uniform mesh with $\Delta x = 0.01\mathrm{m}$ and a constant time step of $\Delta t = 0.001\mathrm{s}$ is used for all the simulations. Regular waves are generated at the upwave end and a non-reflecting wave boundary condition is also specified. At the downwave end, a sponge layer is specified to reduce wave reflection. Six test conditions are selected to validate the model. The wave height at a gage is calculated from the recorded data using zero up-crossing method (Nwogu and Demirbilek 2001). In each simulation, the drag coefficient, C_d, is the only parameter that needs to be calibrated. By trial and error and following MAPE, the calibrated values of the drag coefficient for all the test cases are determined. Figure 10 shows the comparisons of the calculated and measured wave heights for all the six cases. In Fig. 10, the origin is located at G2. The calculated wave heights show wave reflection in the front of the vegetation zone, declining subsequently due to the resistance of vegetation. An error analysis on predicting wave heights at different gage points is summarized in Table 7. It should be noted that gauges G3 and G4 show more errors, but these errors are in a millimetre scale.

Figure 10 shows that the drag coefficients used in the present model are significantly high. The same Boussinesq model was applied to simulate different sets of experimental observations in Wu (2007) and exactly similar trend was found. The 1D Boussinesq model requires significantly larger value of C_d when compared to the analytical models of Dalrymple et al. (1984) and Méndez and Losada (2004), and the vertical 2D model of Wu et al. (2013). If the drag force due to vegetation term used by different models is carefully analysed, it can be found that the analytical and the vertical 2D models use the local velocity squared to compute the drag force, whereas the 1D Boussinesq model uses the depth-averaged velocity squared. Therefore, it is obvious that the calibrated C_d value in the depth-averaged model should be larger than that in the analytical and vertical 2D models to get the same amount of total drag force and energy dissipation in the vertical line.

6 Conclusions

This paper presents a shock-capturing scheme based one-dimensional Boussinesq wave model to simulate wave attenuation due to vegetation. The model uses the extended Boussinesq equations proposed by Madsen and Sørensen (1992). The system of equations is arranged in such a way that shock-capturing capability can be achieved in the model using an approximate Riemann solver (Shiach and Mingham 2009). The governing equations are discretized using a second-order explicit scheme in time and up to fourth-order accurate method in space through a piecewise linear reconstruction of the conserved variables. The effect of vegetation is included in the momentum equation as a source term in the form of a drag force. The drag force expression considers plant characteristics, such as geometry, stem density and spatial coverage, to properly represent the physics of the processes.

Table 6 Laboratory wave configurations used in the simulation

Configuration	Wave height (m)	Period (s)	d/L
(a)	0.066941	1.2	0.322428
(b)	0.065852	1.4	0.249571
(c)	0.065327	1.6	0.204288
(d)	0.067961	1.4	0.249571
(e)	0.085179	1.6	0.204288
(f)	0.080980	1.2	0.322428
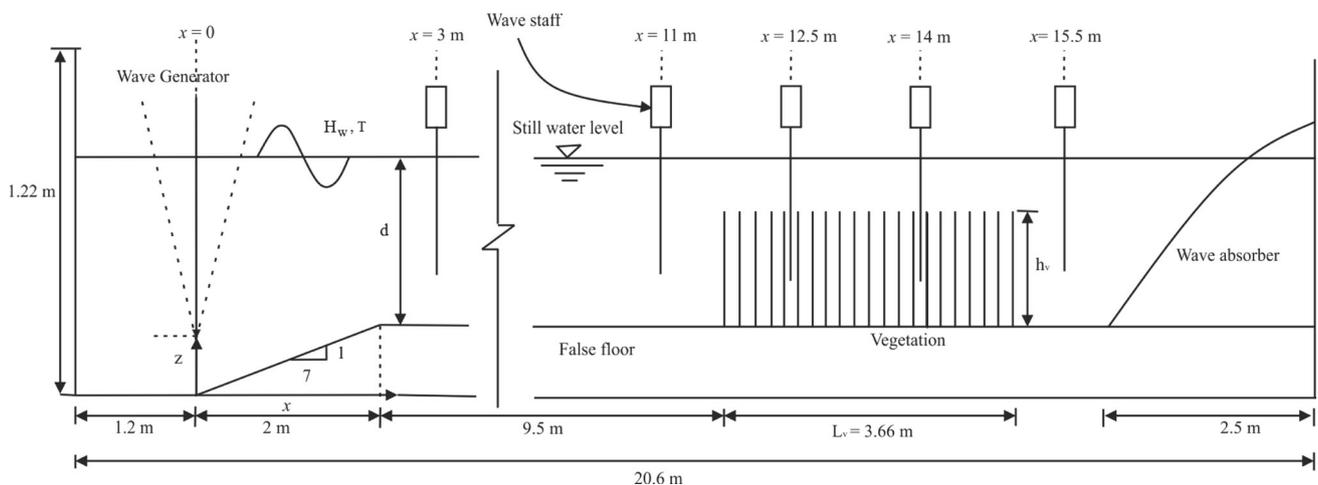
Fig. 9 Definition sketch of the experiment setup
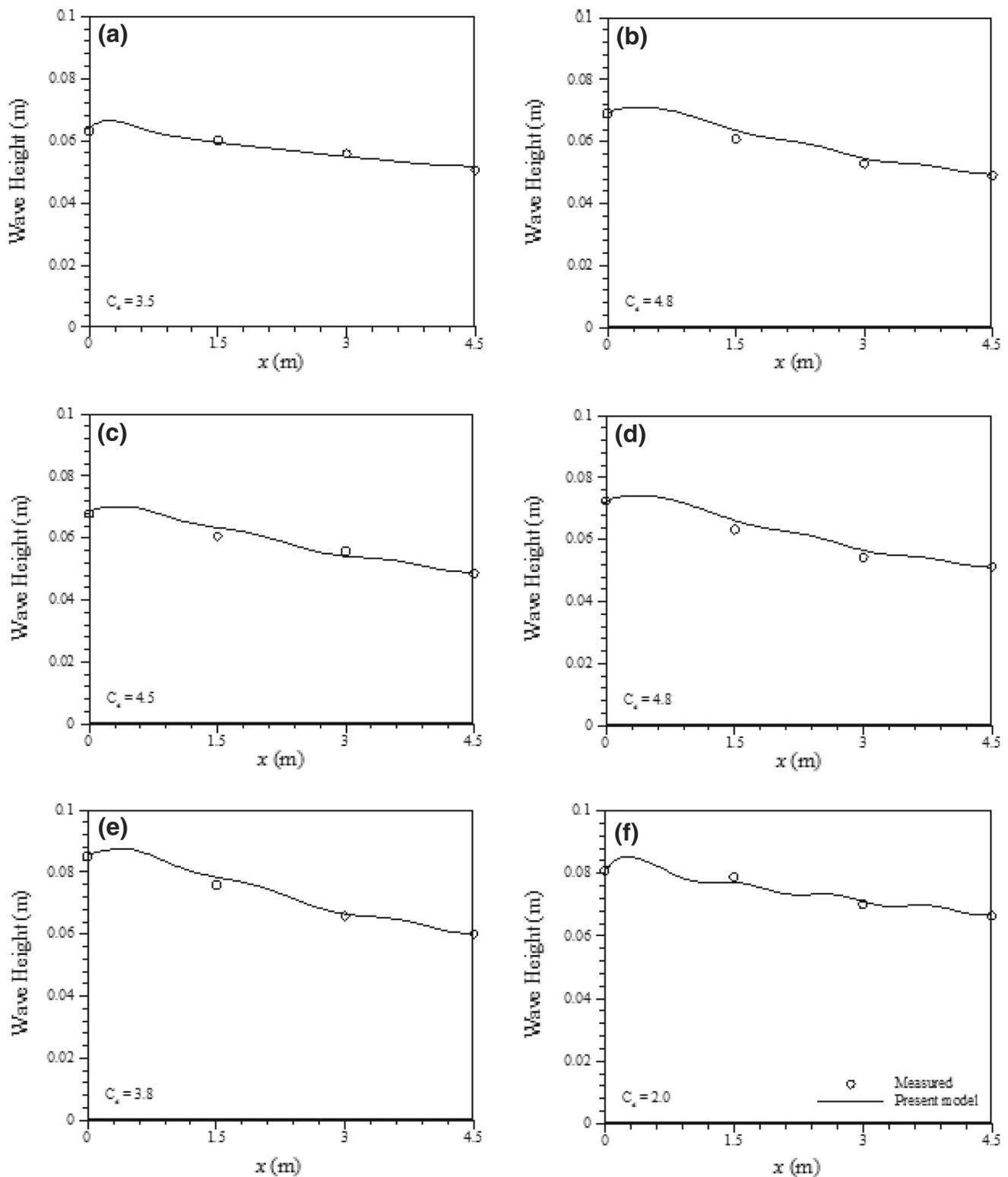
Fig. 10 Variation of wave heights along the flume for wave configurations (**a**–**f**)

The numerical model is first verified against the analytical solutions reported in literature and validated with the laboratory data on wave propagation over a submerged bar. Good

agreement between observed and computed water surface elevations at different observation stations is obtained. The model is then validated with the laboratory data on wave

Table 7 Error values in predicting wave height

Experiment	% Error in wave height			
	G2	G3	G4	G5
(a)	1.94	1.83	3.65	0.71
(b)	1.39	4.60	3.20	0.77
(c)	1.95	4.45	3.22	0.43
(d)	0.69	4.54	4.15	0.45
(e)	0.94	3.31	1.06	0.17
(f)	0.99	2.25	1.28	0.30

attenuation by vegetation and applied to reproduce wave attenuation by cylindrical vegetation in a wave flume. Six more laboratory test cases are presented and the wave heights at several gauges are compared with the observed values. Results indicate that the model can predict wave attenuation due to vegetation with reasonable accuracy. However, it is found that the 1D Boussinesq model requires larger drag coefficient value compared to analytical and vertical 2D models mainly due to the difference in depth-averaged and local velocities. This study opens up a future scope to study the importance of vertical velocity profile on the drag coefficient. The study can be carried out for different vegetation density and types and for different incident wave conditions. Further improvements to the model will consider propagation of breaking waves in real world scenarios and extension to 2D model.

References

Asano T, Tsutsui S, Sakai, T (1988) Wave damping characteristics due to seaweed. In: Proceedings of the 35th coast. engrg. conf. in Japan, Japan Society of Civil Engineers (JSCE), pp 138–142 **(in Japanese)**

Augustin LN, Jennifer LI, Patrick L (2009) Laboratory and numerical studies of wave damping by emergent and near-emergent wetland vegetation. Coast Eng 56(3):332–340

Camfield FE (1983) Wind wave growth with high friction. J Water Port Coast Ocean Eng 109(1):115–117

Carrier GF, Greenspan HP (1958) Water waves of finite amplitude on a sloping Beach. J Fluid Mech 4:97–109

Dalrymple RA, Kirby JT, Hwang PA (1984) Wave diffraction due to areas of energy dissipation. J Waterway Port Coast Ocean Eng 110(1):67–79

Dingemans MW (1987) Verification of numerical wave propagation models with laboratory measurements. Report H228 part 1. Delft hydraulics

Harten A, Lax PD, van Leer B (1983) On upstream differencing and Godunov-type schemes for hyperbolic conservation laws. SIAM Rev 25(1):35–61

Hu K, Mingham CG, Causon DM (2000) Numerical simulation of wave overtopping of coastal structures using the non-linear shallow water equations. J Coast Eng 41:433–465

Knutson PL, Brochu RA, Seelig WN, Inskeep M (1982) Wave damping in Spartina alterniflora marshes. Wetlands 2:87–104

Kobayashi N, Raichlen AW, Asano T (1993) Wave attenuation by vegetation. J Water Port Coast Ocean Eng 199(1):30–48

Kuiry SN, Wu W, Ding Y, Wang SSY (2012) A shock-capturing one-dimensional model for long wave run-up. ISH J Hydraul Eng 18(2):65–79

Li CW, Yan K (2007) Numerical investigation of wave–current–vegetation interaction. J Hydraul Eng 133(7):794–803

Lynett PJ, Wu TR, Liu PL-F (2002) Modeling wave runup with depth-integrated equations. J Coast Eng 46:89–107

Madsen PA, Murray R, Sørensen OR (1991) A new form of Boussinesq equations with improved linear dispersion characteristics. Coast Eng 15:371–388

Madsen PA, Sørensen OR (1992) A new form of the Boussinesq equations with improved linear dispersion characteristics. Part 2. A slowly-varying bathymetry. Coast Eng 18:183–204

Méndez FJ, Losada IJ (2004) An empirical model to estimate the propagation of random breaking and nonbreaking waves over vegetation fields. Coast Eng 51:103–118

Nwogu O, Demirbilek Z (2001). Bouss-2d: a Boussinesq wave model for coastal regions and harbors. Coastal Hydraulics Laboratory, Report no. ERDC/CHL TR-01-25

Nwogu O (1993) An alternative form of the Boussinesq equations for nearshore wave propagation. J Water Port Coast Ocean Eng 119(6):618–638

Nwogu OG, Demirbilek Z (2001) BOUSS-2D: a Boussinesq wave model for coastal regions and harbors. Technical report ERDC/CHL TR-01-25, U.S. Army Engineer Research and Development Center, Vicksburg, MS

Ozeren Y, Wren DG (2011) Experimental investigation of surge and wave reduction by vegetation (phase I). National Sedimentation Laboratory Research Report No, Oxford, MS, p 73

Peregrine DH (1967) Long waves on a beach. J Fluid Mech 27(4):815–827

Price WA, Tomlinson KW, Hunt JN (1968) The effect of artificial seaweed in promoting the build-up of beaches. Proceedings of 11th conference on coastal engineering, vol 1. ASCE, London, pp 570–578

Que Y-T, Xu K (2005) The numerical study of roll-waves in inclined open channels and solitary wave runup. Int J Numer Meth Fluids 50:1003–1027

Schutten J, Dainty J, Davy AJ (2004) Wave-induced hydraulic forces on submerged aquatic plants in shallow lakes. Ann Botany 93:333–341

Shi F, Kirby JT, Harris JC, Geiman JD, Grilli ST (2012) A high-order adaptive time-stepping TVD solver for Boussinesq modelling of breaking waves and coastal inundation. Ocean Model 43–44:36–51

Shiach JB, Mingham CG (2009) A temporally second-order accurate Godunov-type scheme for solving the extended Boussinesq equations. Coast Eng 56:2–45

Stone BM, Shen HT (2002) Hydraulic resistance of flow in channels with cylindrical roughness. J Hydraul Eng 128(5):500–506

Thomas LH (1949) Elliptic problems in linear differential equations over a network. Lab report, Watson Sci. Comput, Columbia University, New York

Thuy NB, Tanimoto K, Tanaka N (2010) Flow and potential force due to runup tsunami around a coastal forest with a gap, experiments and numerical simulations. Sci Tsunami Haz 29(2):43–69

Tonelli M, Petti M (2009) Hybrid finite volume—finite difference scheme for 2DH improved Boussinesq equations. Coast Eng 56:609–620

Tonelli M, Petti M (2010) Finite volume scheme for the solution of 2D extended Boussinesq equations in the surf zone. Ocean Eng 37:567–582

Wei G, Kirby JT (1995) Time-dependent numerical code for extended Boussinesq equations. J Water Port Coast Ocean Eng 121(5):251–261

Wu W (2007) Computational river dynamics. Taylor & Francis, London

Wu W, Ozeren Y, Wren D, Chen Q, Zhang G, Holland M, Ding Y, Kuiry SN, Zhang M, Jadhav R, Chatagnier J, Chen Y, Gordji L (2011) Investigation of surge and wave reduction by vegetation. Phase I report for SERRI project no. 80037, The University of Mississippi, MS. http://www.serri.org/publications/Documents/Ole%20Miss20Project%2080037%20-%20Final%20Report%20%201%20-31%20March%202011%20%28Wu%29.pdf

Wu W, Zhang M, Yavuz O, Wren DG (2013) Analysis of vegetation effect on waves using a vertical 2D RANS model. J Coast Res 29(2):383–397

Wu Y, Falconer A, Struve J (2001) Mathematical modelling of tidal currents in mangrove fields. Env Mod Soft 16(1):19–29

Yamamoto S, Kano S, Daiguji H (1998) An efficient CFD approach for simulating unsteady hypersonic shock–shock interference flows. Comput Fluids 27(5–6):571–580

Zhan J-M, Yu L-H, Li C-W, Li Y-S, Zhou Q, Han Y (2014) A 3-D model for irregular wave propagation over partly vegetated waters. Ocean Eng 75:138–147

Zhou JG, Causon DM, Mingham CG, Ingram DM (2001) The surface gradient method for the treatment of source terms in the shallow water equations. J Comput Phys 168:1–25